Supplementary Information for

Isotropic 3D Super-resolution Imaging with a Self-bending Point Spread Function

Shu Jia, Joshua C. Vaughan, Xiaowei Zhuang

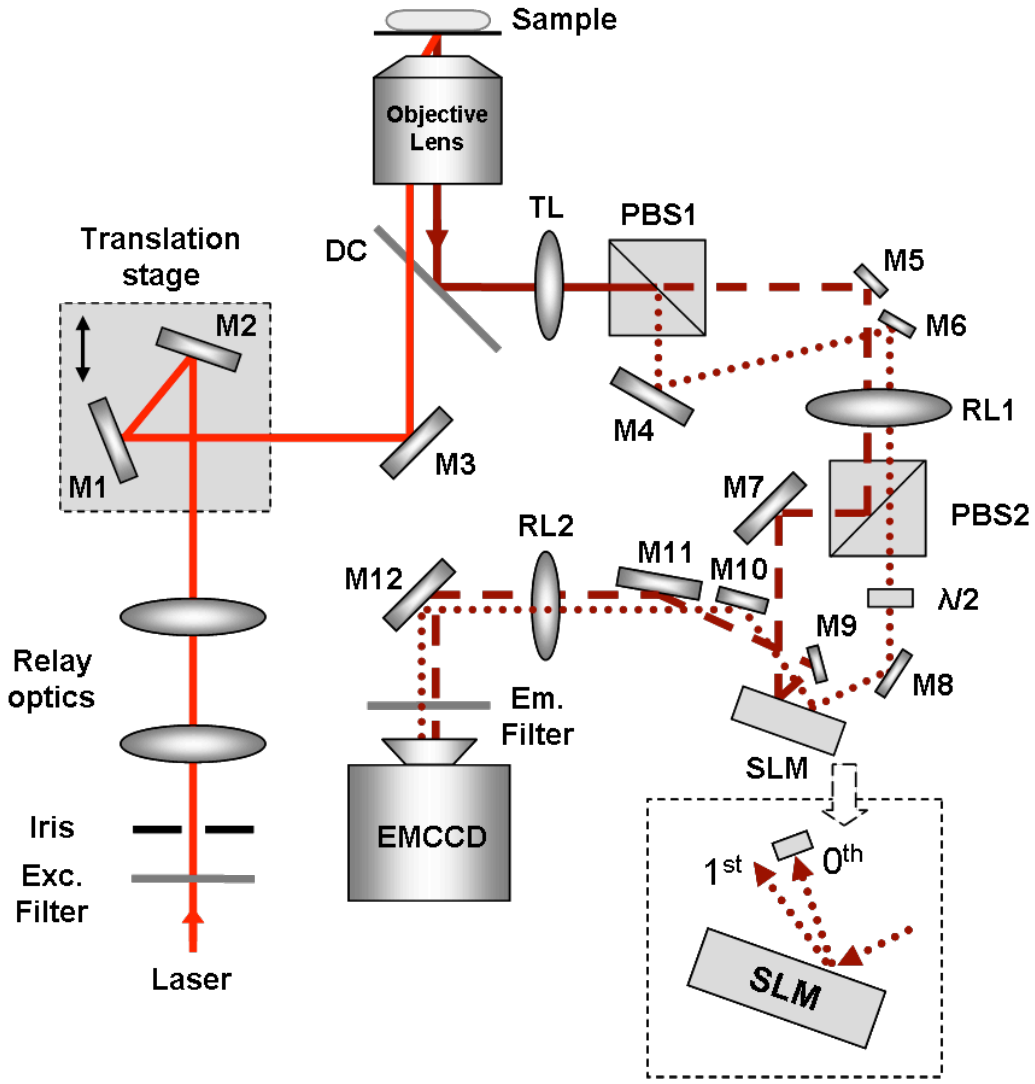

Supplementary Figure 1. Detailed schematic of the optical setup. The set-up was built on a 60 cm x 60 cm breadboard using a compact design. The sample was illuminated by excitation (647 nm) and photoactivation (405 nm) lasers during image acquisition. In the excitation path, the size of the laser beam is adjusted by an **iris** and collimated by **relay optics**. Mirrors **M1** and **M2** are translated by a **translation stage** in order to control the incidence angle between the epi-illumination and TIRF geometry. In the detection path, a polarizing beam splitter **PBS1** first separates the emission into two polarizations, which are propagated through **RL1** and further separated by a second polarizing beam splitter **PBS2**. Experimentally, we found that slightly deviating the two beams oppositely off the center of the 2-inch lens RL1 by ~5 mm helps enlarge the bending angle. Mirrors (**M5**, **M7**) and (**M4**, **M6**, **M8**) independently direct each beam. Because the spatial light modulator (**SLM**) is polarization dependent, the polarization of

one of the beams is rotated by a half-wave plate (**λ/2**) such that both beams are polarization-aligned with the active polarization direction of the **SLM**. The two beams are launched at different incident angles on the **SLM**, resulting in slight difference in beam profiles, which are compensated during the channel alignment between the two channels (see details in Supplementary Figure 5). D-shaped mirrors **M6**, **M9**, and **M10** are used to allow space for two approaching beams. Mirrors **M9, M10**, **M11**, and **M12** are used to project two beams onto separate regions of the **EMCCD**. The optical path lengths of the beams were adjusted to be identical in each section between the tube lens **TL** (200 mm achromatic doublet lens) and the relay lens **RL1** (200 mm achromatic doublet lens), between **RL1** and **SLM**, between **SLM** and another relay lens **RL2** (200 mm achromatic doublet lens), and between **RL2** and **EMCCD**. Any difference can be compensated by an additional parabolic phase on the **SLM** so that the same plane in the sample is in focus on the EMCCD in the two channels (see Supplementary Figure 2). **Exc. (Em.) Filter,** excitation (emission) filter. **DC,** dichroic mirror. The inset shows the divergence of different orders of diffraction on the SLM. The first-order diffraction beam is directed to the imaging path, whereas the zeroth-order diffraction is deviated and blocked from the detection path.

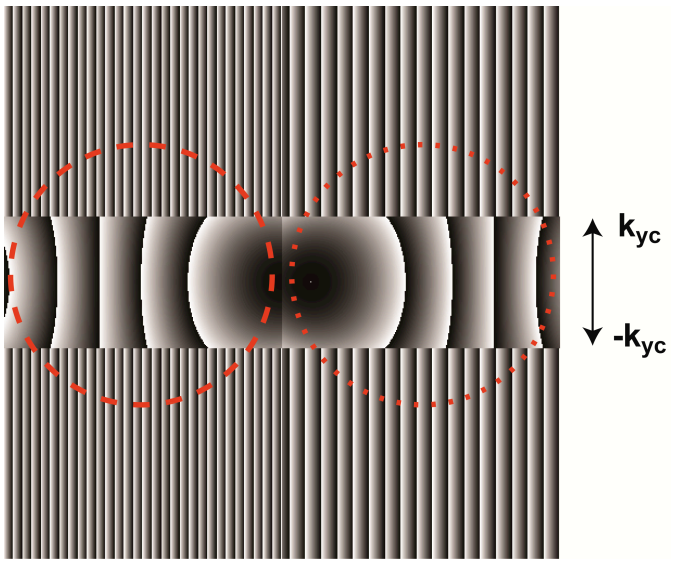

Supplementary Figure 2. Phase pattern used to generate the SB-PSF. The 256 x 256 pixel grayscale image shows the phase modulation that we programmed on the SLM to generate the SB-PSF, with white to black colors denoting gradual phase modulation from 0 to 2π. Dashed and dotted red circles mark approximate areas of the incoming fluorescence light in the left (L) and right (R) channels, respectively. The cubic phase pattern is generated from the expression: $P(k_x,k_y) = A[(k_x + k_y)^3 + (-k_x + k_y)^3] + Bk_x^2 + Ck_y^2$, where $(k_x,\ k_y)$ are pixel numbers between [-127, 128], *A* is the coefficient of the cubic phase term, which determines the self-bending property, the terms $(k_x + k_y)^3$ and $(-k_x + k_y)^3$ ensure that the beam bends along the *x* direction, and *B* and *C* can be independently used to compensate any distortions in the profile of the PSF, which may be induced by astigmatism in the optical system or anisotropy of the Airy beam. *B* and *C* can also be used to adjust the focal position and compensate any propagation length difference in the L and R channels. Experimentally, we adjusted the values of *A*, *B*, and *C* to optimize the performance of the PSF in terms of bending angle, imaging depth and focal position. The optimal values were found to be $A = 10^{-6}$, $B = C = -10^{-3}$. We did not further adjust *B* and *C* to compensate for astigmatism or other beam distortions because the image quality was already adequate. To remove the side-lobes in the SB-PSF, the phase pattern is then truncated at $|k_y| = k_{yc}$, beyond which it is replaced by linear spatial phase gratings in the L and R channels, and hence wavevectors with $|k_y| > k_{yc}$ are not detected. Because

wavevectors $|k_y| > k_{yc}$ are primarily responsible for the side-lobes in an Airy beam generated by the pure cubic spatial phase, removal of these wavevectors, in addition to the optimization of the cubic phase, largely eliminated the side-lobes in the SB-PSF and greatly improved the imaging performance (see Supplementary Figure 3). To separate the above side-lobe-free SB-PSF (first-order diffraction) from unmodulated co-propagating beam (zeroth-order diffraction), an additional linear phase grating (not shown here) was added to the phase pattern shown here, with which different orders of diffractions were deflected at different angles (as shown in the inset of Supplementary Figure 1).

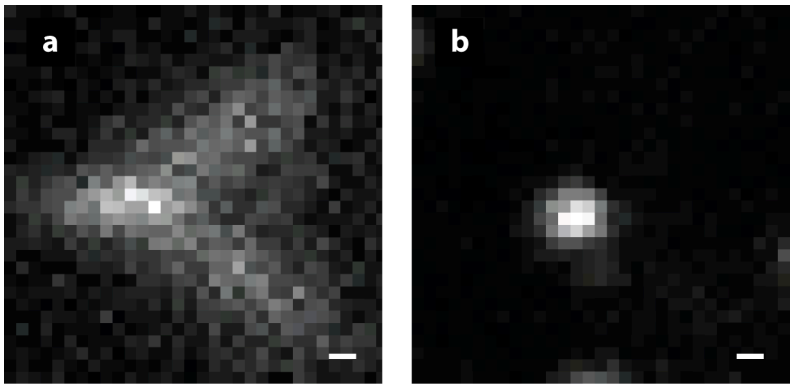

Supplementary Figure 3. Measured transverse profiles of the SB-PSFs generated using the phase masks without and with the additional phase modulation to remove the side-lobes. (a) The transverse profiles of the SB-PSF generated with a SLM that imparted the full cubic phase on the fluorescence emission (phase pattern not shown). (b) The transverse profiles of the SB-PSF generated with a SLM that imparted the truncated cubic phase, which directed the wavevectors $|k_y| > k_{yc}$ out of the detection path (phase pattern shown in Supplementary Figure 2). The PSFs were recorded as the images of 100 nm fluorescent microspheres. The modified Airy beam generated by the new phase modulation shown in Supplementary Figure 2 eliminated the side-lobes, and thereby substantially improved the peak contrast and profile of the PSF and the localization precision of individual emitters. Scale bars, 300nm.

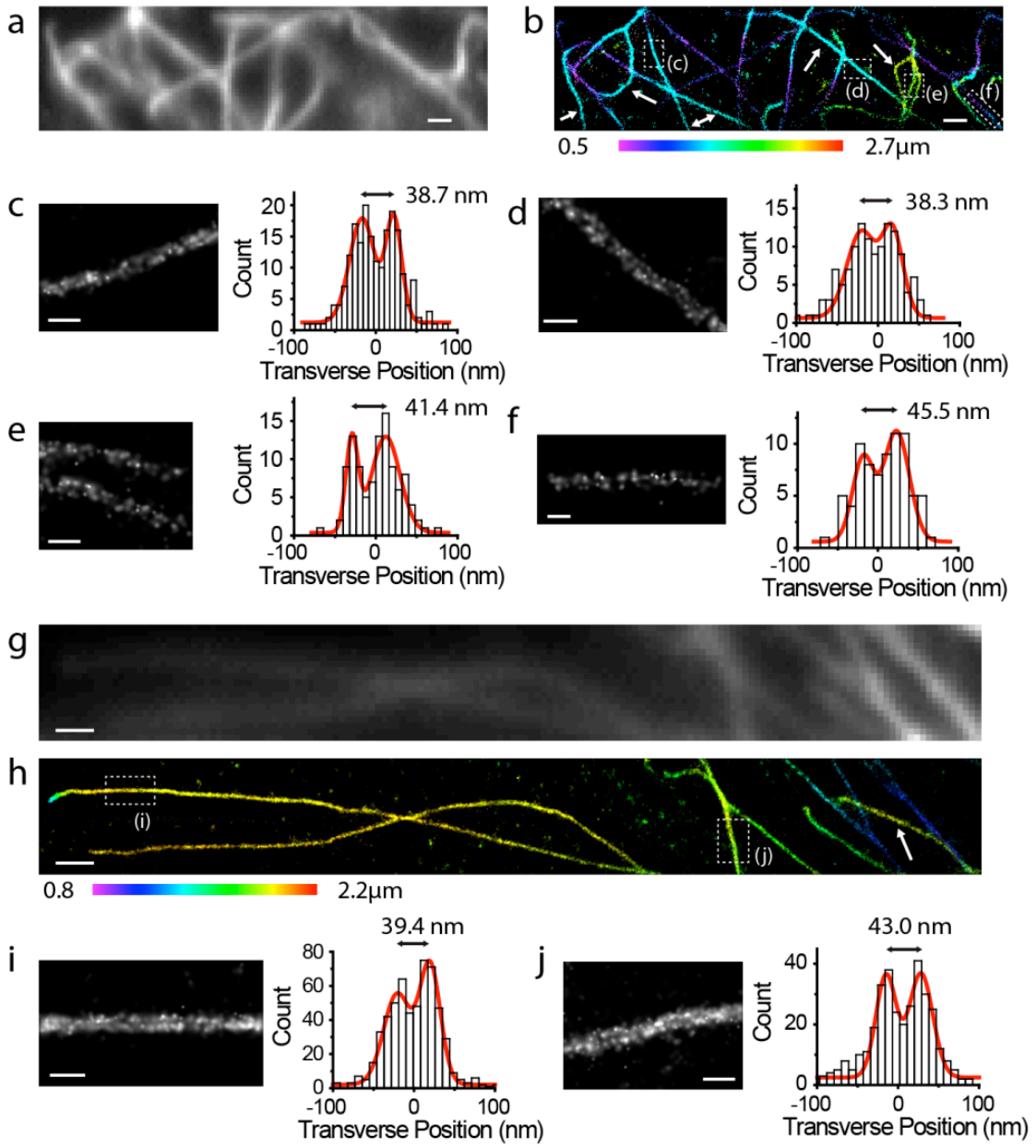

Supplementary Figure 4. STORM imaging of microtubules in cells using SB-PSF and high-density labeling protocol (see Supplementary Methods). Images for two different cells are shown in (a-f) and (g-j), respectively. (a, g) Conventional immunofluorescence images of microtubules in a BS-C-1 cell taken with the standard Gaussian PSF. (b, h) The 3D STORM images of the same areas in (a, g) taken with the SB-PSF. The *z*-position information is color-coded according to the color scale bars. White arrows indicate microtubules that are undetectable in the conventional images in (a) and (g) but are captured in the STORM images in (b) and (h), respectively. (c-f) Zoom-in images and transverse cross-sectional profiles of microtubules in the boxed

regions in (b). In (e), the cross-sectional profile was taken on the bottom microtubule filament. Hollow microtubule structures were well-resolved and the distances between peaks were 38.7 nm, 38.3 nm, 41.4 nm and 45.5 nm, respectively. (i, j) Zoom-in images and transverse cross-sectional profiles of microtubules in the boxed regions in (h). Hollow microtubule structures were well-resolved and the distances between peaks were 39.4 nm and 43.0 nm, respectively. All zoom-in images are orientated along the longer axis of the boxed regions. Scale bars, 1 μm (a, b, g, h); 200 nm (c-f, i, j).

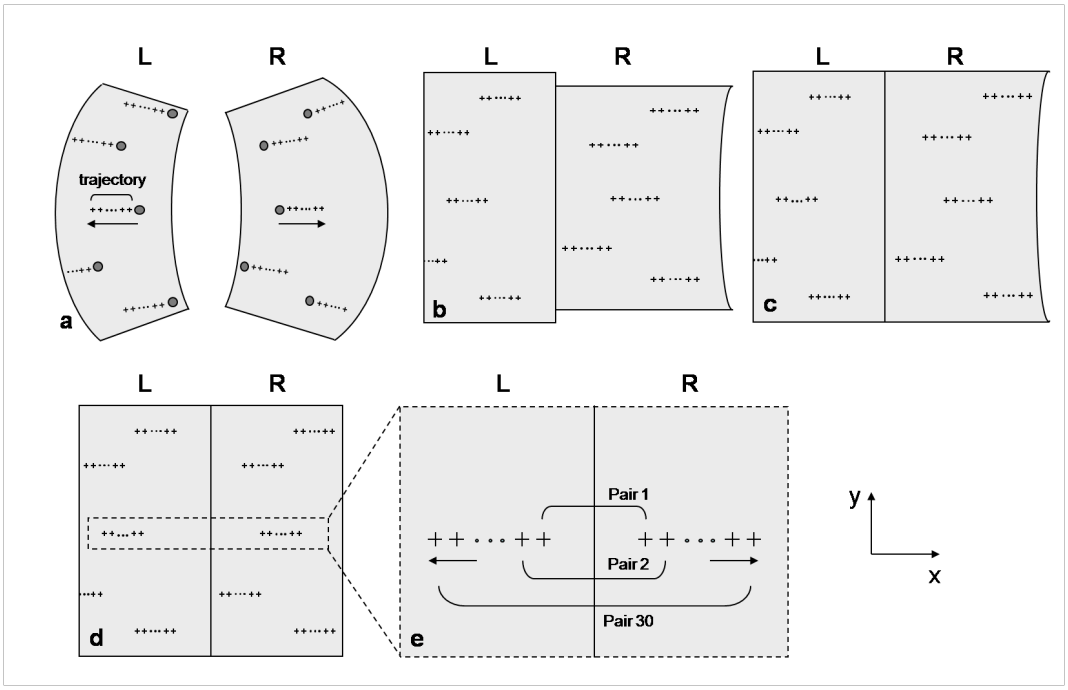

Supplementary Figure 5. Procedures for calibration and alignment of the L and R channels. (a) A sketch of the field of view shown in the L and R channels on the camera and the beads imaged in the two channels. In experiments, there were more than 100 beads uniformly distributed in the field of view. The sample stage was first placed at focal plane, where identical images were recorded in the two channels (images of beads indicated by the gray circles). As the sample was translated axially in 100 nm steps over a >3 μm range, the bead images in the two channels moved in approximately opposite directions as indicated by the arrows. At each height, positions of beads were marked as "+". Each bead thus had a trajectory of positions as a function of axial positions of the sample. Due to aberrations in the optical system, these lateral trajectories were slightly tilted from expected *x* direction, leading to two slightly curved fields of view for the L and R channels after all bead positions recorded at different axial sample positions were stacked (The tilt angles are exaggerated in the plot for illustration purpose). (b) Two curved fields of view were first straightened using third-order polynomial transformations. These transformations keep the lengths of all bead trajectories unchanged but only rotate the angles of the trajectories. We refer to these third-order polynomial transformation matrices as rotation matrices (RMs). (c) We then mapped the *y* positions of the beads in one channel to their corresponding trajectories in the other channel with another third-order polynomial mapping matrix, referred to as vertical matrix (VM). (d) Next, we applied an additional third-order polynomial mapping matrix to make the

bending magnitude, i.e. *x* displacement versus axial positions, uniform (equal to an average bending magnitude) among all beads and symmetric between the L and R channels. We refer to this third-order polynomial mapping matrix as horizontal matrix (HM). (e) After channel calibration and alignment, the bead images in the two channels were identical to each other at any z position of the bead sample, but with exactly anti-symmetric z-dependent lateral bending. The resulting bending distances ($\Delta x = (x_R - x_L)/2$) as a function of the axial positions of the sample were used to generate the calibration curve shown in Figure 1e. Here only the pair of trajectories for one bead is illustrated with pairs 1, 2 and 30 referring to the pairs of bead positions in the L and R channels at axial positions 1, 2 and 30. For STORM imaging, the above calibration process was done prior to STORM image acquisition. For analysis of STORM data, RMs, VM and HM were first applied to drift corrected molecule lists and the calibration curve was used to determine axial positions of individual molecules.

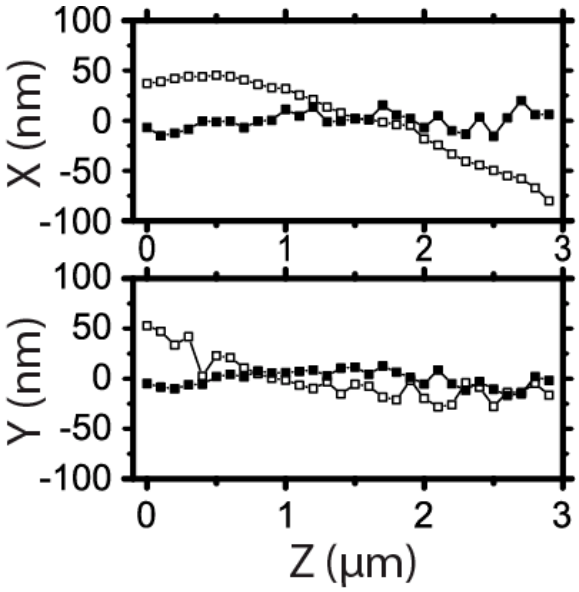

Supplementary Figure 6. Measured lateral positions of a fluorescence microsphere at various preset axial positions before and after channel alignment. The measured x (upper panel) and y (lower panel) positions of a fluorescence microsphere measured at various axial positions of the sample before (open symbols) and after (closed symbols) the L and R channel alignment procedure described in Supplementary Figure 5. The standard deviation of the x-y positions is <8 nm over the entire 3 μm imaging depth after channel alignment.

Supplementary Note 1: Numerical simulation for propagations of SB-PSF and Gaussian PSF.

The numerical simulation of beam propagation is based on the paraxial wave equation:

$$i\frac{\partial U}{\partial z}+\frac{1}{2k}\left(\frac{\partial^2 U}{\partial x^2}+\frac{\partial^2 U}{\partial y^2}\right)=0 \qquad (1)$$

where $U(x,y,z)$ is the slowly-varying wave field, k is the wavenumber, z and (x,y) represents axial and lateral coordinates, respectively. In practice, the initial wave field $U(x,y,0)$ at z = 0 was first defined as either the sum of individual spatial modes for the SB-PSF or the Airy-disk solution for the Gaussian PSF. The propagation of these wave fields was calculated in Fourier space using a linear split-step algorithm over the distance determined by experimental settings, which was then inverse-Fourier transformed to construct the final wave field. Detailed procedures are described below.

For SB-PSF, because fluorescence emission is partially coherent, the incoming wavepacket $W(k_\perp)$ onto the SLM was decomposed into 256 plane-wave composites $W_m(k_\perp)=\exp(imk_\perp)$ (m = 1, 2, …, 256), orienting at different angles enveloped by a Gaussian wavepacket to form $W(k_\perp)=\sum_m \exp(-{k_\perp}^2)W_m(k_\perp)$, where $k_\perp$ represents lateral spatial frequency coordinates k_x and k_y . These individual spatial modes were then multiplied by the cubic phase, $\exp(i[(k_x+k_y)^3+(-k_x+k_y)^3])$ and truncated by a rectangular function $rect(k_{yc})$ in the k_y direction at $|k_y|=k_{yc}$. The wave field H at the SLM is then

$$H(k_\perp)=W(k_\perp)\exp(i[(k_x+k_y)^3+(-k_x+k_y)^3])rect(k_{yc}) \qquad (2)$$

where $rect(k_{yc})$ describes the spatial apodization shown in Supplementary Figure 2. Propagated by the imaging lens RL2 shown in Supplementary Figure 1, the wave field $U(x,y,0)$ on the image plane is the Fourier transform of H,

$$U(x,y,0)=FT(H(k_\perp)). \qquad (3)$$

For the Gaussian PSF, the wave function for a Gaussian PSF $U(x,y,0)$ is described by the exact Airy disk solution $U(x,y,0) = Bessel(r)/r$, where $Bessel(r)$ represents the Bessel function of the first kind as a function of radial coordinate r.

The propagation of wave field $U(x,y,z)$ with the initial wave functions $U(x,y,0)$ was calculated by the split-step algorithm. Specifically, for SB-PSF, mode interactions between individual composites were ignored in light of the incoherence of fluorescence emission. Hence, individual composites were propagated and computed independently and the overall beam intensity was obtained as the incoherent sum of individual intensities. For Gaussian PSF, $U(x,y,z)$ was described by the propagation of the exact Airy disk wave function $U(x,y,0)$.

Eq. (1) gives

$$\frac{\partial U}{\partial z} = i\frac{1}{2k}\left(\frac{\partial^2 U}{\partial x^2} + \frac{\partial^2 U}{\partial y^2}\right) = i\frac{1}{2k}\nabla_\perp^2 U \tag{4}$$

Calculating the Fourier transform of both sides of the wave equation (4) leads to

$$\frac{\partial \widetilde{U}}{\partial z} = i\frac{1}{2k}(i2\pi k_\perp)^2\widetilde{U} = -i\frac{1}{2k}(2\pi k_\perp)^2\widetilde{U} \tag{5}$$

where $\widetilde{U}(k_\perp, z)$ is the Fourier transform of $U(x,y,z)$. Integrating in Fourier space over a small step dz then leads to

$$\widetilde{U}(k_\perp, z+dz) = \exp\left(-i\frac{1}{2k}(2\pi k_\perp)^2 dz\right)\widetilde{U}(k_\perp, z) \tag{6}$$

The term $\exp\left(-i\frac{1}{2k}(2\pi k_\perp)^2 dz\right)$ determines the evolution of the wave field in the Fourier space at every step of propagation. The process was repeated over the desired distance.

At any propagation distance $z + dz$, the wave field in the spatial domain U is then the inverse Fourier transform of $\widetilde{U}$.

Supplementary Note 2: Lateral bending of the SB-PSF.

According to the model of a coherent Airy beam[1, 2], the bending trajectory is described as:

$$\Delta x' = Az'^2 = \frac{1}{2\sqrt{2}k^2 x'^3_0} z'^2 \tag{7}$$

where Δx' and z' are lateral bending and axial propagation distance, respectively, of the beam measured in terms of coordinates on the image plane, A is the bending coefficient, $k = 2\pi/\lambda$ is the wavenumber and x'_0 describes the size of the main lobe. The full width at half maximum (FWHM) of the intensity profile of the main lobe of is $1.6 \cdot x'_0$. ($\Delta x'$, z') may be easily related to the coordinates on the object plane (Δx, z) using $x'_0 = Mx_0$, $\Delta x' = M\Delta x$ and $z' = M^2 z$, where M is the magnification of the imaging system[3]. Hence,

$$\Delta x = \frac{1}{2\sqrt{2}k^2 x_0^3} z^2 \tag{8}$$

In our experiment, with $z = 3\mu m$, $k = 2\pi / 700nm = 9\mu m^{-1}$, $x_0 \approx 250nm$, the lateral bending Δx is estimated to be $2.53\mu m$. Our experimental observation of $\Delta x = (x_R - x_L)/2 = 2.45\mu m$ (Figure 1e) matches well with this predicted value.

Supplementary Note 3: The photon detection efficiency related to the SLM.

We measured the photon losses due to the use of SLM by imaging fluorescence microspheres and found that implementation of the SB-PSF using the truncated cubic phase pattern on the SLM reduced the number of detected photons to ~2000, which is ~35-40% of the value (5000-6000 photons for Alexa 647 per switching cycle) obtained when the SLM is not used. The losses originated from two sources. Phase wrapping (module 2π) on the pixelated SLM resulted in multiple orders of diffraction, where only the first-order diffraction was used. The unmodulated (zeroth-order) light contributed to a ~50% photon loss. Higher-order diffractions were negligible. Removal of side-lobes by the additional phase modulation (See Supplementary Figures 2 and 3) caused additional photon loss and, as a result, 70-80% of the remaining 50% of light were retained. Methods to improve photon efficiency are discussed in the main text.

Supplementary Methods

Sample preparation for single-molecule characterization. Characterization of the localization precision of single molecules was performed using Alexa 647-labeled donkey anti-rat secondary antibodies, as previously described[4]. In brief, all dye-labeled antibodies for single-molecule characterization measurements use dye-labeling ratios < 1 dye per antibody on average such that most labeled antibody have 1 dye per antibody molecule. Labeled antibodies were immobilized on the surface of LabTek 8-well coverglass chambers. Chambers were pre-cleaned by sonication for 10 min in 1 M aqueous potassium hydroxide, washing with Mili-Q water and blow-drying with compressed nitrogen. Labeled antibodies were adsorbed to the coverglass at a density of ~ 0.1 dye μm^{-2} such that individual dye molecules could be clearly resolved from each other. To assist drift correction during acquisition, fiducial markers (0.2 µm orange beads, F8809, Invitrogen) were loaded to chambers at a final density of ~0.01 microspheres/μm^2 prior to sample preparation.

***In vitro* assembled microtubule preparation.** *In vitro* assembled microtubules were prepared according to the manufacturer's protocol (Cat. # TL670M, Cytoskeleton Inc.). In brief, prechilled 20 µg aliquots of HiLyte 647-labeled tubulin (Cat. # TL670M) were dissolved in 5 µL of a prechilled microtubule growth buffer (100 mM PIPES pH 7.0, 1 mM EGTA, 1 mM Mg Cl_2, 1 mM GTP (BST06, Cytoskeleton), and 10% glycerol (v/v)). After centrifugation for 10 min at 14,000 g at 4°C to pellet any initial tubulin aggregates, the supernatant was incubated at 37°C for 20 min to polymerize microtubules. A stock solution of paclitaxel (TXD01, Cytoskeleton) in DMSO was added to the polymerized microtubules to a final concentration of 20 µM and incubated at 37°C for 5 min to stabilize the microtubules. The sample was then stored at 23 °C in the dark. For imaging, 0.2 µL of the stabilized microtubule stock was diluted into 200 µL of 37°C microtubule dilution buffer (100 mM PIPES pH 7.0, 1 mM EGTA, 1 mM $MgCl_2$, 30% glycerol, and 20 µM paclitaxel), incubated for 5 min in silanized LabTek 8-well chambers (see below) which facilitated microtubule sticking, fixed for 10 min in microtubule dilution buffer fortified with 0.5% glutaraldehyde, and washed 3 times with phosphate-buffered saline (PBS). Prior to use, the LabTek 8-well chambers had been cleaned using the same procedure described above, silanized by incubation with 1% N-(2-aminoethyl)-3-aminopropyl trimethoxysilane (UCT Specialties), 5% acetic acid and 94% methanol for

10 min, and washed with water. Fiducial markers were added to the sample using the same procedure described above.

Immunofluorescence staining of cellular structures. Immunostaining was performed using BS-C-1 cells (American Type Culture Collection) cultured with Eagle's Minimum Essential Medium supplemented with 10% fetal bovine serum, penicillin and streptomycin, and incubated at 37°C with 5% CO_2. Cells were plated in LabTek 8-well coverglass chambers at ~20,000 cells per well 18-24 hours prior to fixation. The immunostaining procedure for microtubules and mitochondria consisted of fixation for 10 min with 3% paraformaldehyde and 0.1% glutaraldehyde in PBS, washing with PBS, reduction for 7 min with 0.1% sodium borohydride in PBS to reduce background fluorescence, washing with PBS, blocking and permeabilization for 20 min in PBS containing 3% bovine serum albumin and 0.5% (v/v) Triton X-100 (blocking buffer (BB)), staining for 40 min with primary antibody (rat anti-tubulin (ab6160, Abcam) for tubulin or rabbit anti-TOM20 (sc-11415, Santa Cruz) for mitochondria) diluted in BB to a concentration of 2 µg/mL, washing with PBS containing 0.2% bovine serum albumin and 0.1% (v/v) Triton X-100 (washing buffer, WB), incubation for 30 min with secondary antibodies (~1–2 Alexa 647 dyes per antibody, donkey anti-rat for microtubules and donkey anti-rabbit for mitochondria, using an antibody labeling procedure previously described[4]) at a concentration of ~2.5 µg/mL in BB, washing with WB and sequentially with PBS, postfixation for 10 min with 3% paraformaldehyde and 0.1% glutaraldehyde in PBS, and finally washing with PBS.

For high-density labeling performed in Supplementary Figure 4, the immunostaining procedure for microtubules, as previously described[4, 5], consisted of washing with PBS, extraction for 1 min with 0.2% Triton X-100 in a pH 7 buffer consisting of 0.1 M PIPES, 1 mM ethylene glycol tetraacetic acid, and 1 mM magnesium chloride, fixation for 10 min with 3% paraformaldehyde and 0.1% glutaraldehyde in PBS, reduction for 5 min with 0.1% sodium borohydride in water, washing with PBS, blocking and permeabilization for 30 min with BB, staining for 40 min with primary antibody (rat anti-tubulin (ab6160, Abcam) diluted to 10 µg/mL in BB, washing with PBS, staining for 60 min with a custom-labeled donkey anti-rat secondary antibodies bearing 1.7 Alexa 647 dyes per antibody diluted to 2.5 µg/mL in BB, washing with PBS, postfixation for 10 min with 3% paraformaldehyde and 0.1% glutaraldehyde in PBS, and finally washing with PBS.

Single-molecule and STORM imaging buffer. All imaging was performed in a solution that contained 100 mM Tris (pH 8.0), an oxygen scavenging system (0.5 mg/mL glucose oxidase (Sigma-Aldrich), 40 µg/mL catalase (Roche or Sigma-Aldrich) and 5% (w/v) glucose) and 143 mM beta-mercaptoethanol.

Supplementary References:

1. Baumgartl, J., Mazilu, M., Dholakia, K. Optically mediated particle clearing using Airy wavepackets. *Nature Photon.* **2,** 675-678 (2008).

2. Polynkin, P., Kolesik, M., Moloney, J. V., Siviloglou, G. A., Christodoulides, D. N. Curved Plasma Channel Generation Using Ultraintense Airy Beams. *Science* **324,** 229-232 (2009).

3. Pawley, J. B. *Handbook of biological confocal microscopy*, 3rd edn. Springer: New York, NY, 2006.

4. Dempsey, G. T., Vaughan, J. C., Chen, K. H., Bates, M., Zhuang, X. Evaluation of fluorophores for optimal performance in localization-based super-resolution imaging. *Nat. Methods* **8,** 193901 (2011).

5. Vaughan, J. C., Dempsey, G. T., Sun, E., Zhuang, X. Phosphine quenching of cyanine dyes as a versatile tool for fluorescence microscopy. *J Am Chem Soc* **135,** 1197-1200 (2013).